Performance analysis of wide bandgap inorganic perovskite for indoor photovoltaics for IoT applications: simulation study

L. Vanitha[1] · Satyajeet Sahoo[2] · R. Thandaiah Prabu[3] · Atul Kumar[4]

Abstract

Indoor Photovoltaics are designed to harness indoor light energy for direct electricity generation. Their availability and ambient energy harvesting potential make them an attractive solution for powering electronics in the Internet of Things (IoT) ecosystem. Pb-free, ambient stable, inorganic perovskite $CsGeI_3$ with a wide bandgap of 1.8 eV is computationally analysed for indoor photovoltaic application. It showed a photovoltaic efficiency of 58% in indoor light emitted diode illumination and 55.7% in compact fluorescent light illumination. The narrow emission spectrum of indoor light sources allows better coverage of the spectrum by a wide bandgap absorber, which lowers thermalization losses and thus reaches higher power conversion efficiency. Indoor photovoltaic (IPV) has different device optimization strategies than outdoor 1 sun illumination optimized devices. The main difference is low photogenerated carrier density due to lower incident photons in dim light, which increases the ratio of trapped electrons to photogenerated electrons. This makes the IPV device more susceptible to shunt resistance and interfacial recombination. The series resistance does not impact IPV device efficiency. The high efficiency demonstrated here paves the way for inorganic wide-bandgap perovskite solar cells to play a significant role in powering indoor electronics for the IoT.

✉ Atul Kumar
   er.atul89@gmail.com

   L. Vanitha
   vanithafredrick@gmail.com

   Satyajeet Sahoo
   drss_ece@vignan.ac.in

   R. Thandaiah Prabu
   thandaiah@gmail.com

1   Department of ECE, S.A. Engineering College, Chennai, Tamilnadu, India

2   Department of ECE, Vignan's Foundation for Science, Technology and Research, Vadlamudi, Guntur, Andra Pradesh, India

3   Department of ECE, Saveetha School of Engineering, Saveetha Institute of Medical and Technical Sciences, SIMATS, Chennai, Tamilnadu, India

4   Department of Electronics and Communications Engineering, Koneru Lakshmaiah Education Foundation, Greenfields, Vaddeswaram, Guntur, Andhra Pradesh 522502, India

Springer

1 Introduction

The evolution of human life and the escalating dependence on electronic devices have necessitated the implementation of the Internet of Things (IoT). The autonomous functioning of homes, offices, and cities is facilitated through sensors connected via wireless internet, which sense and monitor their surroundings, exchange data, process information, and respond through actuators. The growth of IoT has been exponential, weaving a vast network of interconnected devices, including monitoring cameras, connected cars, and home appliances. In 2020, IoT device nodes (sensors, back reflectors, actuators, etc.) surpassed human numbers, reaching 11.3 billion units, with projections indicating a surge to 27 billion by 2025 (Wojciechowski and Forgács 2022; Chen 2019). In the era of IoT, humans increasingly rely on decisions made by machines rather than by humans themselves. The extensive and distributed IoT network demands a substantial power supply. Its distributed nature supports mobile, standalone energy utilities to ensure broad network coverage, reduce latency, minimize energy loss, and enhance overall reliability. Although batteries are the primary power source, their limited lifespan and the need for periodic replacement or recharging outweigh the cost of the IoT devices themselves. Additionally, concerns regarding maintenance reliability and environmental impact diminish the battery perspective (Minnaert and Veelaert 2011). Figure 1a provides a summary of the power consumption of various IoT subsystems. Various wireless sensors and communication protocols require power in the range of 100 mW or less (Feng et al. 2021). Decentralized, standalone power generation technologies such as ambient energy harvesting are proposed as an alternative to batteries. Figure 1b comprehensively summarises various ambient energy harvesting techniques and their respective power densities. Among these techniques, thermoelectricity, piezoelectricity, airflow, ambient radio
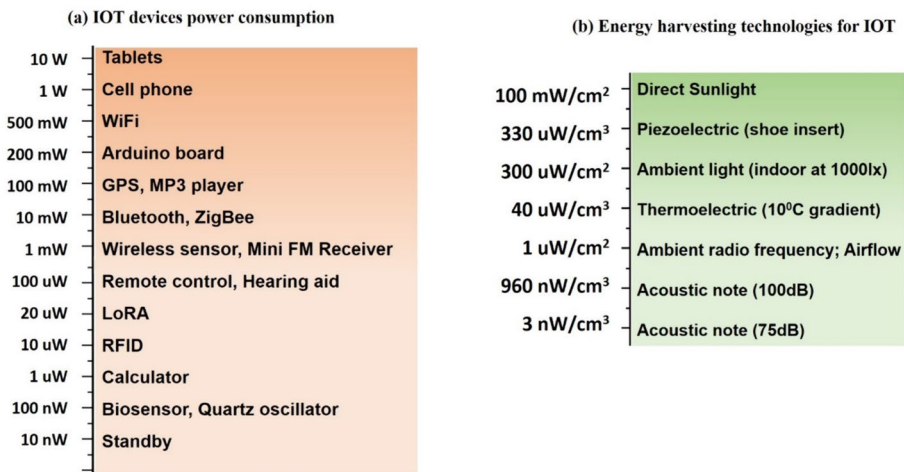

Fig. 1 **a** Power consumption of various electronic devices/sensors in the IoT ecosystem. **b** The power density of various ambient energy harvesting technologies. (Feng et al. 2021; Nasiri et al. 2009; Hwang and Yasuda 2023; Turkevych et al. 2021)

frequency, acoustics, and indoor photovoltaic (IPV) are deemed promising and suitable alternatives (Feng et al. 2021; Nasiri et al. 2009; Hwang and Yasuda 2023; Turkevych et al. 2021). Photovoltaics stand out due to their higher power density, relatively mature technology, and ample illumination available in indoor spaces—where a significant portion of IoT devices are typically located. Light brightness is quantified in luminous flux intensity, measured in lux (lx). Indoor light typically ranges from 100 to 1000 lx, in contrast to the AM1.5G luminance of approximately 120,000 lx (standard outdoor irradiance of 100 mWcm^{-2}). The light irradiation intensity targeted by solar cells for IoT devices is thus a mere 1/1000 of sunlight (Konagai and Sasaki 2020). Consequently, lux serves as a performance evaluation condition specification for IPV devices (Venkateswararao et al. 2020). The general indoor luminance levels vary, with houses typically having 100 lx, office spaces at 500 lx, commercial showrooms at 1000 lx, and surgical rooms at 10,000 lx (Polyzoidis et al. 2021; Jahandar et al. 2021). Figure 2a categorizes indoor spaces based on their illumination intensity, with the Y-axis representing the IPV power density potential of these areas. Figure 2b compares the AM1.5 spectrum with the spectra of light emitted diode (LED) and compact fluorescent light (CFL), illustrating the potential power density in both outdoor and indoor illumination settings. Indoor illumination operates on the principles of incandescence (tungsten and halogen) and luminescence (LED, CFL).

IPV is highly potential candidate as an 15% efficient IPV device under LED illumination of 1000 lx (~ 300 µW cm^{-2}) provide ~ 0.45 mW output power for a 10 cm^2 module. (Johnny Ka Wai et al. 2020; Yan et al. 2022) It is to be noted that the Shockley–Queisser (SQ limit) for outdoor sun air mass AM1.5G is 33%, whereas the IPV efficiency goes as high as 57–58% for LED illumination. The narrow emission spectrum of artificial light sources allows better coverage of the spectrum by a single bandgap absorber, thus resulting in higher efficiency. (Johnny Ka Wai et al. 2020) Sect. 2 describes the simulation methodology utilized for the performance optimization of IPV. IPV have distinct conditions such as low illumination intensity and, consequently, low photogenerated carrier density. Section 3 summarises the optimized efficiency with respect to band gap and recombination under indoor conditions.
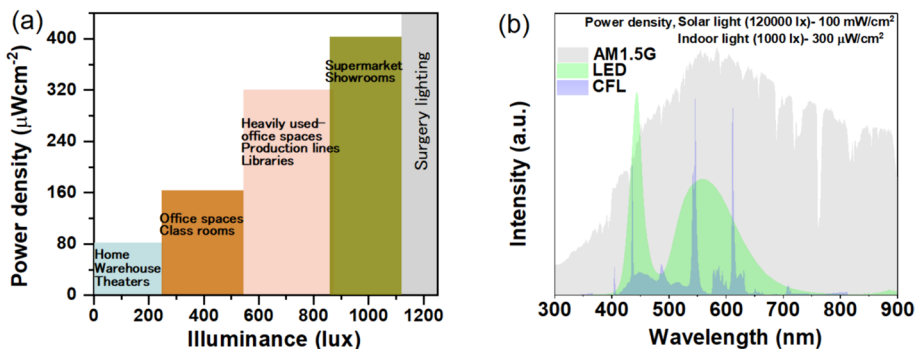

Fig. 2 a The photovoltaic power generation potential of indoor spaces with respect to lux intensity and categorizes various indoor spaces/locations with their respective intensity. (Polyzoidis et al. 2021; Jahandar et al. 2021; Johnny Ka Wai et al. 2020) **b** The comparative emission spectrum of 1 Sun AM1.5G (https://www.nrel.gov/grid/solar-resource/spectra-am1.5.html) and indoor illumination sources LED, CFL in the visible spectral range (https://lspdd.org/database)

2 Simulation methodology

The global air mass (AM 1.5G) terrestrial solar spectrum from American Society for Testing and Materials (ASTM G173-03) is accessible through NREL (https://www.nrel. gov/grid/solar-resource/spectra-am1.5.html). In our analysis of indoor photovoltaics, we focused on two prevalent sources of indoor illumination: light-emitting diodes (LED) and compact fluorescent lights (CFL). Based on manufacturers' practices, commercially available LED/CFL exhibits slight variations in spectral distribution, power density, and luminance. The Lamp Spectral Power Distribution Database (LSPDD) provides a spectral power distribution database for various indoor illumination devices, including LED, CFL, incandescent, etc., catering to domestic, commercial, industrial, streetlight, and medical applications (https://lspdd.org/database). LSPDD compares, summarizes, and maintains a database of artificial illumination sources from different manufacturers. Commercially available LEDs come with various specifications of colour temperatures. Temperatures below 3000 K have a higher content of yellow and red composition, producing warm white light as shown in Fig. 3a–d. Around 5000 K, the spectrum has a blue shift, creating cool white light, aligning well with the human eye's sensitivity, which peaks at 550 nm for green light. CFL spectra at different colour temperatures are depicted in Fig. 4a–d. Higher colour temperatures in CFL show an increased green portion, aligning better with eye sensitivity, while the blue portion also rises at higher colour temperatures. For optimizing solar cell structure and performance in indoor PV, CFL, and LED spectrum conditions, we employed SCAPS version 3.3.1, a 1D Poisson-Schrodinger solver developed by Prof. M. Burgelman from the University of Gent, Belgium (Burgelman et al. 2000; Gomathi
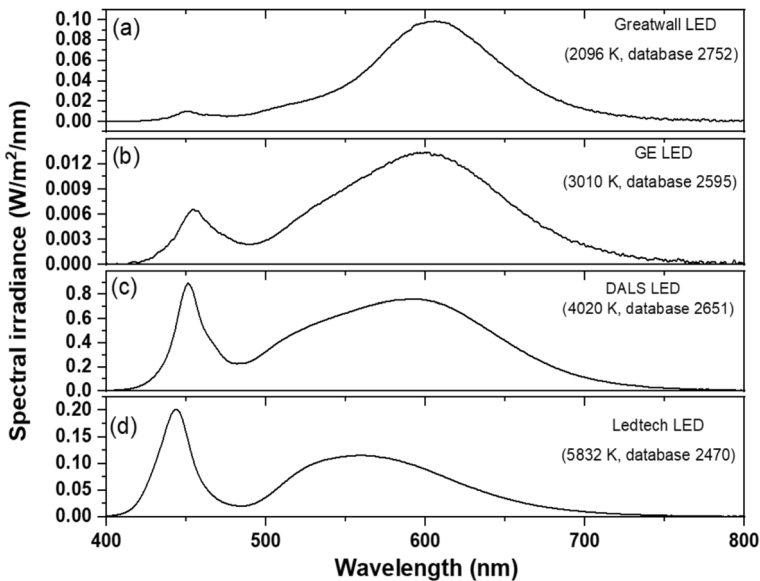

Fig. 3 The spectral irradiance of indoor LED with different colour temperatures of **a** 2000 K, **b** 3000 K, **c** 4000 K, **d** 6000 K. The lower colour temperature (< 3000 K) is warm white, and the higher colour temperature is cool white. The blue shift and infrared compositions decreased with high colour temperature. The LED spectrum is plotted from reference 15, please see text for LED detail
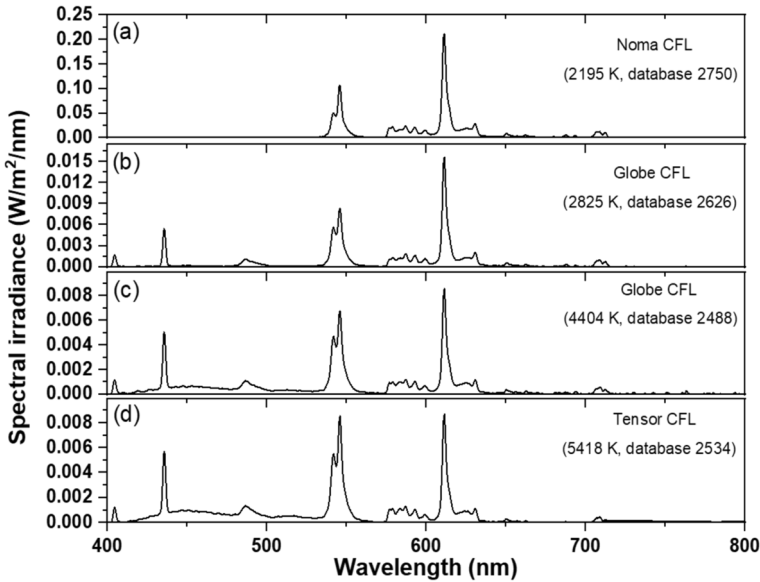
Fig. 4 The spectral irradiance of indoor CFL with different colour temperatures of **a** 2195 K, **b** 2825 K, **c** 4404 K, **d** 5418 K. The high colour temperature with cool white light has a higher blue composition. The CFL spectrum is plotted from reference 15, please see text for CFL detail

et al. 2023; Kumar et al. 2021; Prabu et al. 2023). Simulation results, summarized here, can be reproduced using material parameters from Table 1 and conditions summarized in the respective descriptions in Sect. 3. All the numerical output presented here are output of SCAPS software package.

In exploring indoor photovoltaics, $CsGeI_3$, a wide-band inorganic, Pb-free, and stable perovskite, is considered. The perovskite with Ge substitution attains a degree of stability by developing a Ge-rich native oxide layer, roughly 5 nm in thickness, on the surface of the absorber at the interface between the perovskite and the hole transport layer (HTL), which acts as a protective shield against further oxidation of the inner atoms. (Chen et al.

Table 1 Material parameters for wide band gap IPV device (Chen et al. 2019; Liu et al. 2020; Chen 2018; Krishnamoorthy et al. 2015; Thandaiah Prabu et al. 2023)

Parameters/material	p^+ HTL	$CsGeI_3$ (Chen 2018)	n^+ ETL
Thickness (µm)	0.2	0.4	0.2
Bandgap (eV)	3.2	1.8 (Chen 2018)	3
Electron affinity (eV)	2	4	4
Conduction band density of state, (cm^{-3})	2×10^{19}	2×10^{18}	1.2×10^{19}
Valence band density of state, (cm^{-3})	10^{19}	10^{19}	1.8×10^{19}
Electron thermal velocity (cm/s)	10^7	10^7	10^7
Hole thermal velocity (cm/s)	10^7	10^7	10^7
Electron mobility μ_e,	0.0001	20	0.001
Hole mobility μ_h (cm^2/Vs)	0.0001	20	0.001

2019; Liu et al. 2020) The resulting inorganic perovskite from mixed Sn-Ge systems exhibits greater stability than pure Sn or Pb-based perovskite. Utilizing Ge in mixed Sn-Ge perovskites offers several advantages: (i) Ge -based perovskite shows wide bandgap tunability. (Chen 2018) (ii) Ge's lower atomic mass compared to Pb and Sn leads to higher power density. (iii) $CsGeI_3$ exhibits higher structural tolerance factors than $CsSnI_3$, indicating greater stability of $CsGeI_3$. Moreover, $CsGeI_3$ remains stable at room temperature and retains stability with slight rhombohedral distortion up to 350 °C.

It offers a tunable bandgap in the range of 1.6–3 eV with halide composition variation (Chen 2018; Krishnamoorthy et al. 2015; Thandaiah Prabu et al. 2023). $CsGeI_3$, is structurally stable with a Goldschmidt tolerance factor of 0.92–0.95. (Thandaiah Prabu et al. 2023) Ge-based perovskite is selected to alleviate concerns about the toxicity of lead, while the inclusion of inorganic cations (Cs, Ge) serves to mitigate stability concerns associated with hybrid organic–inorganic perovskites. These concerns encompass issues such as hygroscopicity, volatility, as well as thermal and chemical instability linked to organic cations. The IPV device has an Au/HTL/$CsGeI_3$/ETL/FTO structure with an absorber stacked between a highly doped hole transport layer (HTL) and an electron transport layer (ETL). Spiro-OMeTAD and TiO_2 are HTL and ETL respectively.

3 Results and discussion

3.1 Impact of bandgap on IPV efficiency

The detailed balance efficiency limit of indoor photovoltaics (η_{IPV}) was calculated for the spectral photon flow of an LED, CFL and, as a reference, standard ASTM-G173 AM1.5 global spectrum. The indoor domestic light sources LED, and CFL (available from various manufacturers, at various colour temperatures and (in LSPDD (https://lspdd.org/datab ase)) are Greatwall LED (2096 K, database 2752), GE LED (3010 K, database 2595), DALS LED (4020 K, database 2651), Ledtech LED (5832 K, database 2470), Noma CFL (2195 K, database 2750), Globe CFL (2825 K, database 2626), Globe CFL (4404 K, database 2488) and Tensor CFL (5418 K, database 2534).

The calculation of the indoor efficiency limit followed the detailed balance Shockley–Queisser model. (Shockley and Queisser 1961) IPV efficiency depends upon the indoor light spectrum, and power output depends upon both the indoor light spectrum and luminance level. The detailed balance efficiency is calculated from the portion of the incident spectrum absorption by the absorber, unavoidable intrinsic radiative recombination, and the fill factor (FF) loss associated with non ideality of J-V curve. The AM1.5G spectrum spans 300 n–4000 nm, which is unfeasible to fully capture by any single band gap absorber, giving rise to spectrum loss of non-absorption and thermalization. The luminescence-based indoor lightings such as LED and CFL have relatively narrower emission spectra, which allows the entire spectrum to be captured by a single band gap. This allows the lowering of spectrum loss of non-absorption and thermalization. Therefore, IPV is supposed to have higher efficiency than outdoor photovoltaics. However, the power output in IPV remains lower than the latter. Under ideal conditions, major efficiency limiting factors for IPV are the intrinsic radiative recombination and the fill factor (FF) loss. (Shockley and Queisser 1961) Fig. 5 shows the efficiency as a function of the bandgap for various LED illumination (marked by different bold lines) and AM1.5G spectrum (marked by a faint star). For LED spectrum efficiency, it maximizes in the band gap range of 1.8–1.9 eV.
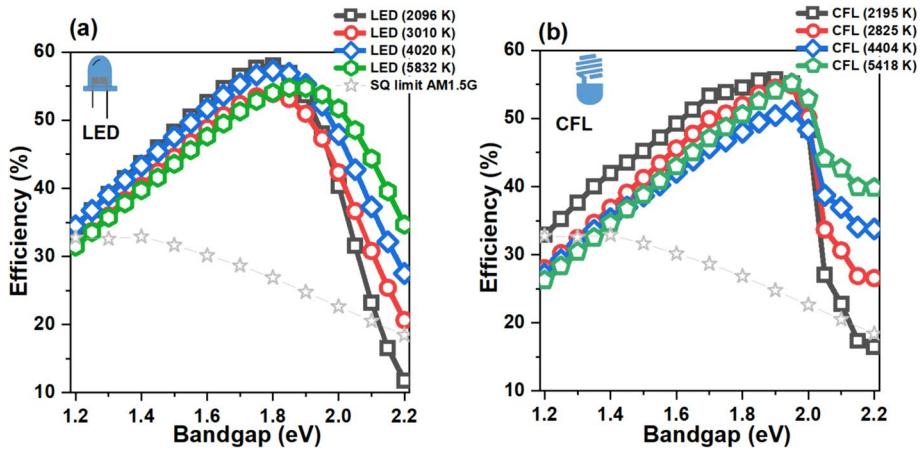
Fig. 5 a The detailed balance calculation of photovoltaic performance for various incident LED spectrum indoor conditions. The efficiency maximizes at 58% for the 1.8 eV band gap. The SQ limit performance (marked in faint stars) for the AM1.5G spectrum is plotted to compare the efficiency of indoor PV and outdoor PV. **b** The detailed balance calculation of photovoltaic performance for various incident CFL spectrums. The efficiency maximizes at 55.7% for a 1.9 eV bandgap

The maximum efficiency is 58% at a 1.8 eV band gap for Greatwall LED (2096 K, database 2752) and 55.7% for a 1.9 eV bandgap for Noma CFL (2195 K, database 2750). For comparison, SQ limit efficiency for outdoor photovoltaic is also plotted, which showed maximum efficiency of 33% at 1.4 eV. We summarises the theoretical maximum efficiency, corresponding bandgap, incident integrated optical power densities and the corresponding output electrical power density for all sources in Table 2.

3.2 EQE of IPV device

The external quantum efficiency (EQE) of wide band gap HTL/CsGeI$_3$/ETL device is simulated in Fig. 6a. The quantum efficiency peaks between 350 and 650 nm, with a cut-off at around 650 nm (corresponding to the band gap of 1.9 eV); higher wavelengths (> 650 nm) are lost to non-absorption. External quantum efficiency (EQE) also commonly referred to as the IPCE (incident photon to current conversion efficiency). It is the number of electrons leaving the cell (as current I_{ph}) divided by the total number of photons incident on the cell. (Brus 2012) EQE empirically given as

$$EQE(\lambda) = \frac{I_{ph}/q}{P_{in}/h\nu} \tag{1}$$

The simulated EQE is high because we have taken (i) constant absorption coefficient and (ii) the optimised configuration (with all passivated interfaces), which results in 100% EQE in visible spectrum and (iii) transmission of the top contact is assumed to be ideal i.e. 100%. We have taken absorber band gap 1.8 eV for EQE calculation as at this band gap efficiency maximizes, and it corresponds to the maximum utilization of incident spectrum. The wide emission spectrum of LED is shown in the background, which extends from 500 to 700 nm. The external quantum efficiency delineates the spectral response of the photovoltaic device, serving as a tool to compute the net achievable current density (J_{in}). The

Table 2 The maximum efficiency, corresponding bandgap, incident integrated optical power densities and the output electrical power for all sources

| S.No	Source	Maximum theoretical efficiency	Corresponding bandgap at which highest efficiency is achieved	Input power (incident power)	Output power
1	Noma CFL (2195 K, database 2750)	55.713%	1.9 eV	0.542 mWcm^{-2}	0.302 mWcm^{-2}
2	Globe CFL (2825 K, database 2626)	55.196%	1.95 eV	47 µWcm^{-2}	25.942 µWcm^{-2}
3	Globe CFL (4404 K, database 2488)	51.089%	1.95 eV	43 µWcm^{-2}	21.968 µWcm^{-2}
4	Tensor CFL (5418 K, database 2534)	55.196%	1.95 eV	46 µWcm^{-2}	25.390 µWcm^{-2}
5	Greatwall LED (2096 K, database 2752)	58.039%	1.8 eV	2.21 mWcm^{-2}	1.282 mWcm^{-2}
6	GE LED (3010 K, database 2595)	53.838%	1.8 eV	0.41 mWcm^{-2}	0.220 mWcm^{-2}
7	DALS LED (4020 K, database 2651)	57.252%	1.8 eV	2.41 mWcm^{-2}	1.379 mWcm^{-2}
8	Ledtech LED (5832 K, database 2470)	54.743%	1.85 eV	4.14 mWcm^{-2}	2.266 mWcm^{-2}
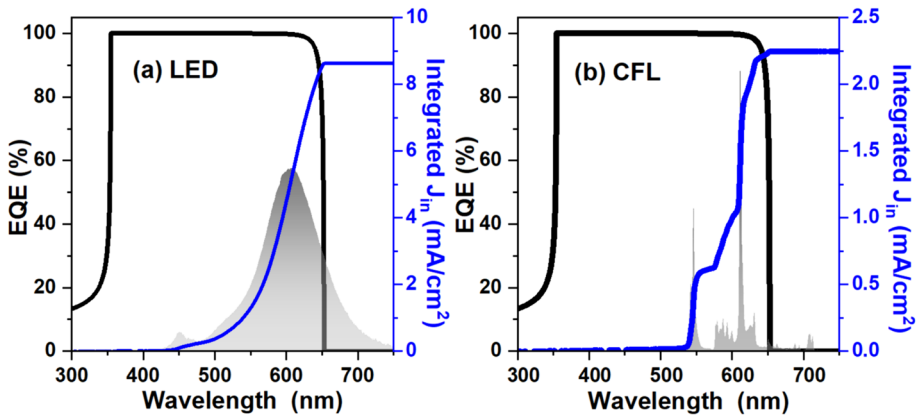
Fig. 6 **a** The simulated EQE plot and the calculated current from EQE for incident LED spectrum under indoor conditions. The led spectrum is shown in the background (not to scale). **b** The simulated EQE plot and the calculated current from EQE for incident CFL illumination under indoor conditions. The CFL spectrum is shown in the background (not to scale)

corresponding maximum short circuit current obtainable from LED illumination is calculated from EQE and named integrated current (J_{in}). The net current can be calculated by integrating the product of EQE and the incident LED spectrum. The empirical equation of J_{in} and EQE dependence is given as

$$J_{in, EQE} = \int q\, EQE(\lambda) S(\lambda) d\lambda \tag{2}$$

where S(λ) is the incident photons spectrum. (Saliba and Etgar 2020) The detailed balance limit value of integrated current comes out to be ~ 8.7 mA/cm^2. The EQE of the same device under CFL illumination is plotted in Fig. 6b. The emission spectra of CFL, shown in the background, have a narrow emission line at 550 nm and 625 nm, as shown in Fig. 6b. The calculated maximum achievable current, integrated current J_{in} from CFL illumination, is calculated and plotted. The integrated current stands at 2.25 mA/cm^2. The J_{in} from CFL is far smaller than J_{in} from LED due to the narrow spectrum of CFL.

3.3 Impact of resistance on IPV

The current–voltage (I-V) characteristics of solar cell under illumination is empirically given as (Gholizadeh et al. 2017)

$$J = J_{ph} - J_O \left(e^{\frac{q(V+JR_S)}{nkT}} - 1 \right) - \frac{V + JR_S}{R_{Sh}} \tag{3}$$

The effective series resistance in a device is often represented by a constant lumped R_s. The series resistance represents electrical ohmic loss arising from the flow of photogenerated current through various layers of the solar cell, contact resistance between the metal contacts. (Warashina and Ushirokawa 1980) The ideal value of series resistance is zero. It is a parasitic effect that cannot be eliminated but can be reduced by better design. The shunt resistance R_{Sh} is the resistance to internal recombination current. It represents a leakage pathway for light-generated current, due to internal recombination, and material defects.

Internal recombination current arises in practical devices due to defect-induced recombination, non-ideal material, and interfacial and electrical properties. (Shina et al. 2019) Very high values of shunt resistance are desirable for solar cells. The effect of a shunt resistance is particularly severe at low light levels since there will be less light-generated current. The calculation method of series and shunt resistance is summarised in supplementary file as supplementary Table 1.

The simplest equivalent circuit model of a photovoltaic cell based on Eq. 3 is single diode model (SDM) as shown in Fig. 7. (Chan et al. 1986; Tivanov et al. 2005; Zhang et al. 2011). SDM consists of four different elements, a current source (J_{ph}) representing light absorption, a diode representing heterojunction, series resistance (R_S) and shunt resistance (R_{Sh}).

Under indoor conditions, the IPV performance becomes sensitive to R_{Sh} and impact of R_S is limited. Kim et al. summarised the equation that explains IPV behaviour. The solar cell Eq. (2) in outdoor solar illumination is modified to (under low illumination i.e. small J_{ph}) (Kim et al. 2020)

$$\lim_{j \to 0} V = \frac{nKT}{q} \left[\ln \left(\frac{J_{sc} - \frac{V}{R_{Sh}}}{J_o} + 1 \right) \right] \tag{4}$$

Monika et al. summarised the minimum value of R_{Sh} for IPV devices as $R_{Sh}^{min} \approx \frac{V_{oc}}{J_{sh}}$ as J_{ph} is low the value of R_{Sh}^{min} is increased. (Freunek et al. 2013) We summarised the modified J-V equation applicable for indoor photovoltaic in as supplementary file as supplementary Table 2.

The impact of shunt resistance (R_{Sh}) on the device is simulated in Fig. 8. R_{Sh} signifies internal recombination and leakage current, where the ideal scenario is maximum R_{Sh} (ideally ∞) and minimum R_S (ideally 0) for optimal photovoltaics performance and maximum output power. Figure 8a shows the simulated J–V characteristics of IPVs with different R_{Sh}. J-V plot shows slight decay with a large variation in R_{Sh} from 10^6 to 10^3 Ωcm^2 for outdoor sun conditions. (Lübke et al. 2023) Under indoor conditions, the impact of R_{Sh} differs significantly. Figure 8b shows substantial decay in J-V characteristics for R_{Sh} variation from 10^6 to 10^3 Ωcm^2. The area under the J-V plot was reduced to almost zero for low shunt resistance. R_{Sh} becomes more crucial for indoor low-illuminance photovoltaic
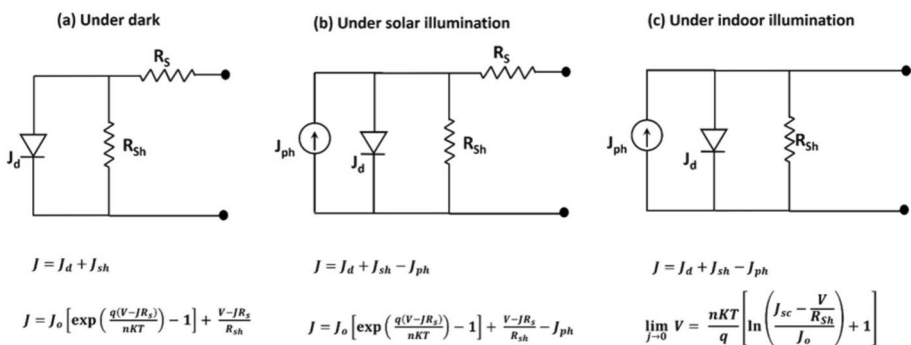

(a) Under dark

$$J = J_d + J_{sh}$$

$$J = J_o \left[\exp\left(\frac{q(V - JR_s)}{nKT} \right) - 1 \right] + \frac{V - JR_s}{R_{sh}}$$

(b) Under solar illumination

$$J = J_d + J_{sh} - J_{ph}$$

$$J = J_o \left[\exp\left(\frac{q(V - JR_s)}{nKT} \right) - 1 \right] + \frac{V - JR_s}{R_{sh}} - J_{ph}$$

(c) Under indoor illumination

$$J = J_d + J_{sh} - J_{ph}$$

$$\lim_{j \to 0} V = \frac{nKT}{q} \left[\ln \left(\frac{J_{sc} - \frac{V}{R_{Sh}}}{J_o} \right) + 1 \right]$$

Fig. 7 The equivalent circuit diagram of device **a** under dark, **b** outdoor solar illumination and **c** indoor illumination
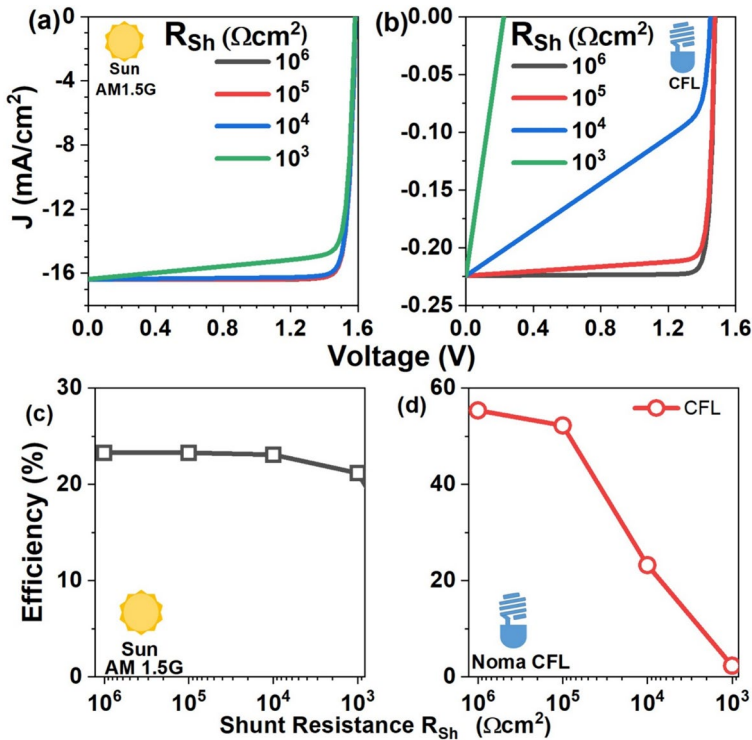
Fig. 8 **a** The JV curves for different values of shunt resistance in outdoor sun conditions. **b** The IPV JV curves show degrading performance for shunt resistance variation. The efficiency as a function of shunt resistance in case of **c** outdoor sun conditions and **d** indoor (IPV) conditions for (Noma CFL (2195 K, database 2750) (https://lspdd.org/database)

performance. (Hwang and Yasuda 2023; Freunek et al. 2013; Lübke et al. 2023; Suthar et al. 2023; Steim et al. 2011).

This peculiar behaviour of IPV device could be elucidated by attributing it to trap-assisted recombination where prominence of R_{Sh} becomes predominant in the carrier recombination processes, particularly at low carrier densities. The low luminance corresponds to a reduced photogenerated carrier density; this condition has important consequences on the recombination process of the IPV device. The criticality of trap-mediated charge recombination arises from the heightened ratio of trapped electrons to photogenerated electrons, leading to an increase in internal recombination. Therefore, increasing R_{Sh} by suppressing trap-assisted recombination is vital for achieving high PCEs for IPVs. Figure 8c–d shows the efficiency is stable for outdoor PV and steeply falls for indoor LED and CFL luminance with decreasing R_{Sh}. These fundamental design principles deviate significantly from the guidelines set for traditional solar cells, with R_s no longer exerting a substantial influence on the overall J–V characteristics. (Glowienka and Galagan 2022).

The impact of series resistance on the device is simulated in Fig. 9. Under high illuminance (outdoor sun), the pehotovoltaic characteristics are mainly governed by R_S, and the impact of R_{Sh} is very limited. It is evident that the smallest possible R_S (ideally 0) is preferred for ideal photovoltaic performance for 1sun illumination. Figure 9a shows the
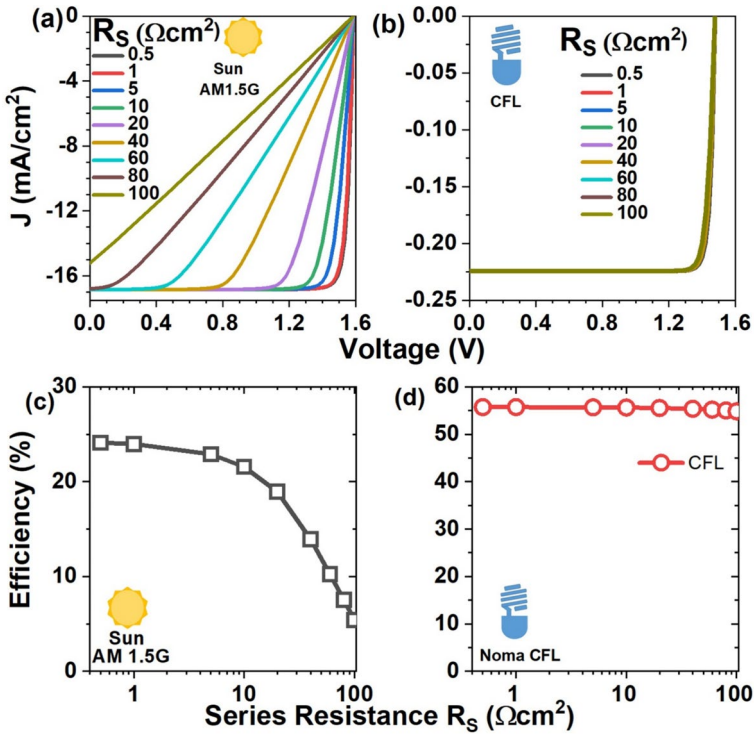
Fig. 9 a The J-V curves show decaying performance with increasing series resistance for outdoor sun conditions. **b** The IPV J-V curves show stable performance for series resistance variation. The efficiency as a function of series resistance in case of **c** outdoor sun conditions and **d** indoor (IPV) conditions for (Noma CFL (2195 K, database 2750) (https://lspdd.org/database)

simulated J–V characteristics of IPVs with different R_S. J-V plot shows strong dependence on series resistance and observed steep decay with large variation in R_S from 0.5 to 100 Ωcm^2 for outdoor sun conditions. Under indoor conditions, the impact of R_S is very limited. The comparative plot highlights the effects that are quite different from those found under outdoor conditions. Evidently, the J_{SC} in outdoor conditions is almost ten times of the J_{SC} in indoor conditions; due to the high photogenerated carrier density under high illumination, the device becomes highly sensitive to series resistance (R_S). Under high illumination, a high photogenerated carrier's density is thus highly sensitive to series resistance. Figure 9c–d shows the efficiency is stable for indoor PV and steeply falls for outdoor illuminance with increasing R_S. These foundational design principles diverge significantly from the guidelines set for traditional (outdoor) solar cells, with R_{Sh} becoming a critical design parameter.

The crucial performance parameter that is affected by low illuminance is FF. Figure 10 shows the comparative FF for outdoor AM1.5 illuminance and indoor CFL illuminance. Under outdoor illuminance, FF shows 10% decay for decreasing shunt resistance, whereas it falls steeply with over 60% decay for indoor illumination, as shown in Fig. 10a. Series resistance decays outdoor FF and has negligible impact on IPV, as shown in Fig. 10b. FF dependence on shunt resistance is a crucial design aspect to be considered for IPV performance optimization. High FF and R_{Sh} could be achieved by minimizing leakage current

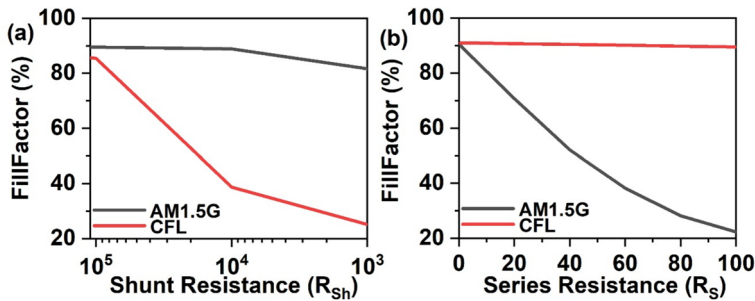**Fig. 10 a** Fill factor in outdoor sun conditions remains stable against variation in shunt resistance, whereas it falls steeply for IPV. **b** IPV shows a stable fill factor for the large variation in series resistance, whereas the fill factor in outdoor PV conditions falls steeply with increasing series resistance

induced by pinholes in the photoactive layer and interfacial recombination. (Meng et al. 2021).

The performance of IPV depends upon (1) the spectral composition of indoor light and (2) the dominating recombination mechanism under low photogenerated carrier density. The spectral characteristics of indoor light sources, which differ from the AM1.5 spectrum of outdoor sunlight. This led to distinct optimal bandgap and maximum power conversion efficiency. These parameters diverge from those specified by the Shockley-Queisser limit for outdoor solar cells. Low incident illuminance leads to lower photogenerated carrier density, which increases the ratio of trapped electrons to photogenerated electrons. Thus, trap-mediated charge recombination becomes critical in IPV. Addressing this necessitates meticulous interface engineering to mitigate recombination losses of the photogenerated carriers in IPV.

4 Conclusion

Inorganic perovskite $CsGeI_3$, with a wide bandgap of 1.8 eV, showed a photovoltaic efficiency of 58% in indoor LED illumination and 55.7% in compact fluorescent light (CFL) illumination. We highlighted indoor photovoltaic (IPV) optimized devices, which are in contrast to 1 sun illumination photovoltaic optimized design. Due to low luminance in dim indoor light conditions, the incident photons are low, which in turn results in low photogenerated carriers. This has important consequences as low photogenerated carrier density increases the ratio of trapped electrons to photogenerated electrons. IPV HTL/$CsGeI_3$/ETL device efficiency and FF have a strong dependence on shunt resistance and are independent of series resistance, which is unlike one sun device. It is apparent that optimal photovoltaic performance and maximum output power require shunt resistance ($R_{Sh} > 10^6$ Ωcm^2) and independent of series resistance values as high as 100 Ωcm^2.

Declarations

Conflict of interest The authors declare no competing interests.

Ethical approval Not applicable.

References

Brus, V.V.: On quantum efficiency of nonideal solar cells. Sol. Energy **86**, 786–791 (2012)

Burgelman, M., Nollet, P., Degrave, S.: Modelling polycrystalline semiconductor solar cells. Thin Solid Films **361–362**, 527–532 (2000)

Chan, D.S.H., Phillips, J.R., Phang, J.C.H.: A comparative study of extraction methods, for solar cell model parameters. Solid-State Electron **29**, 329–337 (1986)

Chen, L.-J.: Synthesis and optical properties of lead-free cesium germanium halide perovskite quantum rods. RSC Adv. **8**, 18396–18399 (2018)

Chen, F.-C.: Emerging organic and organic/inorganic hybrid photovoltaic devices for specialty applications: low-level-lighting energy conversion and biomedical treatment. Adv. Opt. Mater. **7**, 1800662 (2019). https://doi.org/10.1002/adom.201800662

Chen, M., Ju, M.G., Garces, H.F., Carl, A.D., Ono, L.K., Hawash, Z., Zhang, Y., Shen, T., Qi, Y., Grimm, R.L., Pacifici, D., Xeng, X.C., Zhou,Y., Padture N.P.: Highly stable and efficient all-inorganic lead-free perovskite solar cells with native-oxide passivation. Nat. Commun. **10**, 16 (2019). https://doi.org/10.1038/s41467-018-07951-y

Feng, M., Zuo, C., Xue, D.-J., Liu, X., Ding, L.: Wide-bandgap perovskites for indoor photovoltaics. Sci. Bull. **66**, 2047–2049 (2021)

Freunek, M., Freunek, M., Reindl, L.M.: Maximum efficiencies of indoor photovoltaic devices. IEEE J. Photovolt. **3**, 59–64 (2013). https://doi.org/10.1109/JPHOTOV.2012.2225023

Gholizadeh, A., Reyhani, A., Parvin, P., Mortazavi, S.Z.: Efficiency enhancement of ZnO nanostructure assisted Si solar cell based on fill factor enlargement and UV-blue spectral down-shifting. J. Physl. D: Appl. Phys. **50**(18), 185501 (2017). https://doi.org/10.1088/1361-6463/aa6454

Glowienka, D., Galagan, Y.: Light intensity analysis of photovoltaic parameters for perovskite solar cells. Adv. Mater. **34**, 2105920 (2022). https://doi.org/10.1002/adma.202105920

Gomathi, S., Raj, A.G.S., Mishra, C.S., Kumar, A.: Straddling type sandwiched absorber based solar cell structure. Optik **272**, 170354 (2023). https://doi.org/10.1016/j.ijleo.2022.170354

Hwang, S., Yasuda, T.: Indoor photovoltaic energy harvesting based on semiconducting π-conjugated polymers and oligomeric materials toward future IoT applications. Polym. J. **55**, 297–316 (2023)

Jahandar, M., Kim, S., Lim, D.C.: Indoor organic photovoltaics for self-sustainable IoT devices: Progress Challenges and Practicalization. ChemSusChem **14**, 3449–3474 (2021). https://doi.org/10.1002/cssc.202100981

Johnny Ka Wai, H., Yin, H., So, S.K.: From 33% to 57%–An elevated potential of efficiency limit for indoor photovoltaics. J. Mater. Chem. A **8**, 1717–1723 (2020). https://doi.org/10.1039/C9TA11894B

Kim, G., Lim, J.W., Kim, J., Yun, S.J., Park, M.A.: Transparent thin-film silicon solar cells for indoor light harvesting with conversion efficiencies of 36% without photo-degradation. ACS Appl. Mater. Interfaces **12**(24), 27122–27130 (2020). https://doi.org/10.1021/acsami.0c04517

Konagai, M., Sasaki, R.: Bifacial amorphous Si quintuple-junction solar cells for IoT devices with high open-circuit voltage of 3.5V under low illuminance. Prog. Photovolt. **28**, 554–561 (2020). https://doi.org/10.1002/pip.3215

Krishnamoorthy, T., Ding, H., Yan, C., Leong, W. L., Baikie, T., Zhang, Z., Sherburne, M., Li, S., Asta, M., Mathews, N., Mhaisalkar, S.G.: Lead-free germanium iodide perovskite materials for photovoltaic applications. J. Mater. Chem. A **3**, 23829–23832 (2015)

Kumar, A., Singh, N.P., Sundaramoorthy, A.: Comparative device performance of CZTS solar cell with alternative back contact. Mater. Lett.: X **12**, 100092 (2021). https://doi.org/10.1016/j.mlblux.2021.100092

Liu, M., Pasanen, H., Ali-Lçytty, H., Hiltunen, A., Lahtonen, K., Qudsia, S., Smtt, J.-H., Valden, M., Tkachenko, N.V., Vivo, P.: B-site co-alloying with germanium improves the efficiency and stability of all-inorganic tin-based perovskite nanocrystal solar cells. Angew. Chem. Int. Ed. **59**, 22117–22125 (2020)

Lübke, D., Hartnagel, P., Hülsbeck, M., Kirchartz, T.: Understanding the thickness and light-intensity dependent performance of green-solvent processed organic solar cells. ACS Mater. Au **3**, 215–230 (2023)

Meng, Y., Magruder, B.R., Hillhouse, H.W.: On interface recombination, series resistance, and absorber diffusion length in BiI3 solar cells. J. Appl. Phys. **129**, 133101 (2021). https://doi.org/10.1063/5.0034776

Minnaert, B., Veelaert, P.: Efficiency simulations of thin film chalcogenide photovoltaic cells for different indoor lighting conditions. Thin Solid Film **519**, 7537–7540 (2011). https://doi.org/10.1016/j.tsf.2011.01.362

Nasiri, A., Zabalawi, S.A., Mandic, G.: Indoor power harvesting using photovoltaic cells for low-power applications. IEEE Trans. Industr. Electron. **56**, 4502–4509 (2009)

Polyzoidis, C., Rogdakis, K., Kymakis, E.: Indoor perovskite photovoltaics for the internet of things—challenges and opportunities toward market uptake. Adv. Energy Mater. **11**, 2101854 (2021). https://doi.org/10.1002/aenm.202101854

Prabu, R.T., Sahoo, S., Valarmathi, K., Raj, A.G.S., Ranjan, P., Kumar, A., Laref, A.: CsPbI3 perovskite solar cell and decoding its skink feature in J-V curve. Mater. Sci. Semicond. Process. **162**, 107539 (2023). https://doi.org/10.1016/j.mssp.2023.107539

Saliba, M., Etgar, L.: Current density mismatch in perovskite solar cells. ACS Energy Lett. **5**(9), 2886–2888 (2020)

Shin, S.C., You, Y.J., Goo, J.S., Shim, J.W.: In-depth interfacial engineering for efficient indoor organic photovoltaics. Appl. Surf. Sci. **495**, 143556 (2019). https://doi.org/10.1016/j.apsusc.2019.143556

Shockley, W., Queisser, H.J.: Detailed balance limit of efficiency of p-n junction solar cells. J. Appl. Phys. **32**(3), 510–519 (1961)

Steim, R., Ameri, T., Schilinsky, P., Waldauf, C., Dennler, G., Scharber, M., Brabec, C.J.: Organic photovoltaics for low light applications. Sol. Energy Mater. Sol. Cells **95**(12), 3256–3261 (2011)

Suthar, R., Dahiya, H., Karak, S., Sharma, G.D.: Indoor organic solar cells for low-power IoT devices: recent progress, challenges, and applications. J. Mater. Chem. C **11**, 12486–12510 (2023)

Thandaiah Prabu, R., Malathi, S.R., Kumar, A., Al-Asbahi, B.A., Laref, A.: Bandgap assessment of compositional variation for uncovering high-efficiency improved stable all-inorganic lead-free perovskite solar cells. Phys. Status Solidi **220**(6), 2200791 (2023). https://doi.org/10.1002/pssa.202200791

Tivanov, M., Patryn, A., Drozdov, N., Fedotov, A., Mazanik, A.: Determination of solar cell parameters from its current–voltage and spectral characteristics. Sol. Energy Mater. Sol. Cells **87**(1–4), 457–65 (2005)

Turkevych, I., Kazaoui, S., Shirakawa, N., Fukuda, N.: Potential of AgBiI4 rudorffites for indoor photovoltaic energy harvesters in autonomous environmental nanosensors. Jpn. J. Appl. Phys. **60**, SCCE06 (2021). https://doi.org/10.35848/1347-4065/abf2a5

Venkateswararao, A., Ho, J.K.W., So, S.K., Liu, S.-W., Wong, K.-T.: Device characteristics and material developments of indoor photovoltaic devices. Mater. Sci. Eng.: R: Rep. **139**, 100517 (2020). https://doi.org/10.1016/j.mser.2019.100517

Warashina, M., Ushirokawa, A.: Simple method for the determination of series resistance and maximum power of solar cell. Jpn. J. Appl. Phys. **19**(S2), 179 (1980). https://doi.org/10.7567/JJAPS.19S2.179

Wojciechowski, K., Forgács, D.: Commercial applications of indoor photovoltaics based on flexible perovskite solar cells. ACS Energy Lett. **7**, 3729–3733 (2022). https://doi.org/10.1021/acsenergylett.2c01976

Yan, B., Liu, X., Lu, W., Feng, M., Yan, H.J., Li, Z., Liu, S., Wang, C., Hu, J.S., Xue, D.J.: Indoor photovoltaics awaken the world's first solar cells. Sci. Adv. **8**, eadc9923 (2022). https://doi.org/10.1126/sciadv.adc9923

Zhang, C., Zhang, J., Hao, Y., Lin, Z., Zhu, C.: A simple and efficient solar cell parameter extraction method from a single current-voltage curve. J. Appl. Phys. **110**, 064504 (2011). https://doi.org/10.1063/1.3632971